Inorganic Chemistry
Article
pubs.acs.org/IC

Mixed-Spin [2 × 2] Fe_4 Grid Complex Optimized for Quantum Cellular Automata

Benjamin Schneider,[†] Serhiy Demeshko,[†] Sven Neudeck,[†] Sebastian Dechert,[†] and Franc Meyer*,[†]

[†]Institut für Anorganische Chemie, Georg-August-Universität Göttingen, Tammannstrasse 4, 37077 Göttingen, Germany

Ⓢ *Supporting Information*

ABSTRACT: The new pyrazolate-bridged proligand 4-methyl-3,5-bis{6-(2,2′-bipyridyl)}pyrazole (^{Me}LH) has been synthesized. Similar to its congener that lacks the backbone methyl substituent (^{H}LH) it forms a robust Fe^{II}_4 grid complex, $[^{Me}L_4Fe^{II}_4](BF_4)_4$. The molecular structure of $[^{Me}L_4Fe^{II}_4](BF_4)_4\cdot 2MeCN$ has been elucidated by X-ray diffraction, revealing two high-spin (HS) and two low-spin (LS) ferrous ions at opposite corners of the rhombic metal ion arrangement. SQUID and ^{57}Fe Mössbauer data for solid material showed that this [HS−LS−HS−LS] configuration persists over a wide temperature range, between 7 and 250 K, while spin-crossover sets in only above 250 K. According to Mössbauer spectroscopy a [1HS−3LS] configuration is present in solution at 80 K. Thus, the methyl substituent in $[^{Me}L]^-$ leads to a stronger ligand field compared to parent $[^{H}L]^-$ and hence to a higher LS fraction both in the solid state and in solution. Cyclic voltammetry of $[^{Me}L_4Fe^{II}_4](BF_4)_4$ reveals four sequential oxidations coming in two pairs with pronounced stability of the di-mixed-valence species $[^{Me}L_4Fe^{II}_2Fe^{III}_2]^{6+}$ ($K_C = 3.35 \times 10^8$). The particular [HS−LS−HS−LS] configuration as well as the di-mixed-valence configuration, both with identical spin or redox states at diagonally opposed vertices of the grid, make this system attractive as a molecular component for quantum cellular automata.

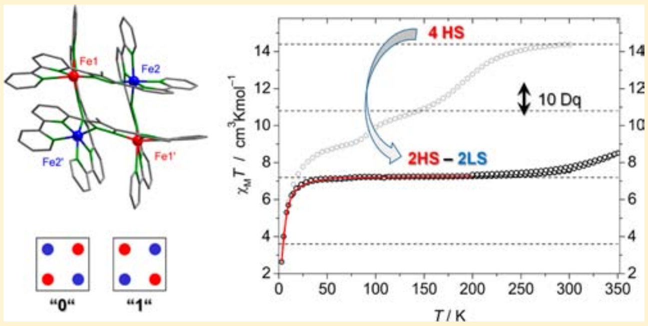

■ INTRODUCTION

The quest for novel molecule-based building blocks for application in molecular electronics is a flourishing field of research, since top-down approaches toward electronic devices are close to reaching the miniaturization limit.[1] In this context, robust and switchable bi- or multistable molecular entities are highly sought after for realizing new types of materials that may be used for transporting or storing information.[2] Mixed-valent compounds as well as spin-crossover compounds, which may switch between high-spin (HS) and low-spin (LS) states,[3] are usually considered promising candidates in this regard. One example for the possible application of such bistable molecules are so-called Quantum Cellular Automata (QCA), which represent an attractive model of alternative logic devices on the nanoscale, potentially offering a new basis for transistorless computing.[4] In QCA, binary information is encoded in the configuration of elementary cells having two stable and energetically degenerate yet distinguishable states, corresponding to 0 and 1, that can be toggled by fields emerging from neighboring cells (Figure 1).[5] Hence, QCA operate without any flow of current or particles, resulting in greatly reduced power dissipation. Using quantum dots for cellular automata was initially envisaged by Lent et al.[6] and implemented using relatively large-scale clusters of metal ions at the corners of a square, but the concept was later extended to single molecules as switchable charge containers.[7,8] In particular, mixed-valent molecules have been discussed as possible candidates for QCA building units,[9,10] provided that the 2-electron, 2-hole di-mixed-valent state is stable with respect to disproportionation and that it ideally is a class II system (according to the Robin and Day classification[11]). Alternatively, the bistable cell states in Figure 1 may be realized in spin-crossover (SCO) complexes with a [HS−LS−HS−LS] configuration. Switching between cell states then requires spin-crossover of each individual metal ion at the corners of the square, while the square's overall spin state (2HS−2LS) remains invariant. This situation differs fundamentally from common approaches toward switchable SCO systems, where changes of overall spin states (preferably abrupt and hysteretic) are sought.[3]

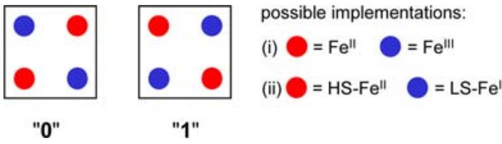

Figure 1. Two states of a four-dot QCA cell.

[2 × 2] grid complexes composed of four metal ions and four mutually perpendicular ditopic ligand strands, featuring a matrix-like array of addressable sites, appear most suited for molecular implementation of the QCA concept.[12] This class of compounds has indeed gained much popularity in the past

Received: August 27, 2013
Published: October 25, 2013

ACS Publications © 2013 American Chemical Society

dx.doi.org/10.1021/ic4021838 | *Inorg. Chem.* 2013, 52, 13230−13237

decade, and numerous [*n* × *n*] grids of different nuclearity, usually formed via self-assembly processes, have meanwhile been reported.[12,13] However, the number of grid-type Fe_4 complexes has remained quite limited,[14−19] despite Fe being a most favorable metal ion for achieving mixed valency (Fe^{II}/Fe^{III}) or spin-crossover. Homometallic Fe_4 grids or squares in the di-mixed-valence $\{Fe^{II}_2Fe^{III}_2\}$ state[16,18,19] as well as all-ferrous Fe_4 grids or squares in the mixed-spin 2HS−2LS state are particularly scarce. Furthermore, the latter complexes mostly undergo gradual or stepwise thermal overall SCO,[14,17−19] which is undesired for QCA implementation requiring a persistent 2HS−2LS configuration.

Recently, we reported a double-switching multistable Fe_4 grid complex that underwent both stepwise spin-crossover and stepwise redox transitions.[19] It was based on the pyrazolate-bridged binucleating ligand $[^{H}L]^-$ that provides two tridentate terpyridine-like binding pockets (Figure 2) and was previously shown to form robust and compact grid complexes with various 3d transition metal ions.[20] The di-mixed-valence species $[^{H}L_4Fe^{III}_2Fe^{II}_2]^{6+}$ as well as the all-ferrous di-mixed-spin species [HS−LS−HS−LS], provided that the metal ions with the same redox or spin state are located at opposite corners of the grid, appeared particularly promising as molecular components for QCA. While the di-mixed-valence species $[^{H}L_4Fe^{III}_2Fe^{II}_2]^{6+}$ indeed proved thermodynamically stable with a large comproportionation constant (K_c = 1.04 × 10^8), all-ferrous $[^{H}L_4Fe^{II}_4]^{4+}$ underwent gradual SCO from the 4HS to the 2HS−2LS configuration upon lowering the temperature from 300 to 50 K and the second SCO to give the 2HS−2LS state was only incomplete. For use in QCA, however, a stable 2HS−2LS state is required over a wide temperature range. We thus set out to slightly increase the ligand field strength by introducing substituents at the periphery of parent $[^{H}L]^-$. This contribution reports the synthesis of the new proligand ^{Me}LH that features a methyl group at the pyrazolate backbone and synthesis and characterization of $[^{Me}L_4Fe^{II}_4]^{4+}$ with particular focus on its redox and magnetic properties.

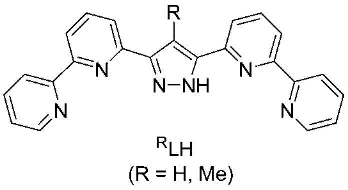

Figure 2. Pyrazolate-bridged binucleating proligands ^{R}LH.

RESULTS AND DISCUSSION

Synthesis and Structural Characterization. The new proligand ^{Me}LH was synthesized following the semiconvergent route that had been developed for parent ^{H}LH.[20] The key intermediate 6-cyano-2,2′-bipyridine, obtained via *N*-oxidation and subsequent cyanation at the 6-position of 2,2′-bipyridine, is functionalized in two different ways (Scheme 1, route 1): basic methanolysis leads to **I**, while a Grignard addition and subsequent hydrolysis gives the corresponding ketone **II**; in the latter step EtMgBr is used for ^{Me}LH, instead of MeMgBr for ^{H}LH (giving **III**). Pseudo-Claisen condensation of **I** and **II** followed by treatment with hydrazine furnishes the target molecule ^{Me}LH. Since in our hands 6-propionyl-2,2′-bipyridine (**II**) showed gradual decomposition upon prolonged storage and the pseudo-Claisen condensation of **I** and **II** gave variable yields, an alternative synthetic route was developed that builds on the already established synthesis of ^{H}LH (Scheme 1, route 2). 1,3-Diketone **IV**, obtained via pseudo-Claisen condensation of **I** and **III** as described,[20] was methylated, and the resulting diketone **V** was then condensed with hydrazine to yield ^{Me}LH. Both routes, being modifications of the original synthesis of ^{H}LH, suggest that different substituents at the 4-position of the resulting pyrazole can be readily introduced by proper choice of the Grignard reagent or alkylating reagent.

For synthesis of the all-ferrous grid complex, ^{Me}LH was dissolved in DMF together with an excess of triethylamine as supporting base or with 1 equiv of NaO*t*Bu. Addition of solid

Scheme 1. Syntheses of the New Proligand ^{Me}LH

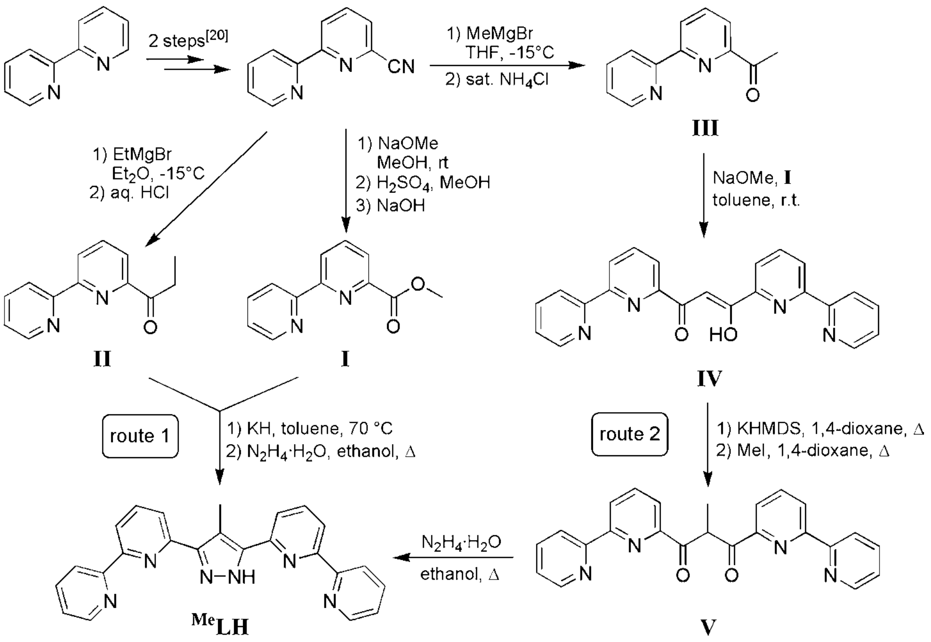

$Fe(BF_4)_2{\cdot}6H_2O$ gave a deep-red solution. After purification by extraction and recrystallization, crystalline material of $[^{Me}L_4Fe^{II}{}_4](BF_4)_4$ was obtained by slow diffusion of Et_2O into a solution of the complex in MeCN.

X-ray diffraction analysis revealed the expected [2 × 2] grid-type molecular structure (Figure 3). Each ferrous ion is found six coordinate in $\{N_6\}$ environment at the grid vertices, bound to two perpendicularly arranged $[^{Me}L]^-$ ligand strands. The overall charge of the complex cation (4+) is balanced by four BF_4^- anions; additionally, at least one MeCN molecule is found in the unit cell. The four metal ions are arranged in a plane to form a rhomb (interior angles 80° and 100°). Two different, crystallographically independent iron centers (Fe1, Fe2) are found with their respective symmetry equivalents Fe1′ and Fe2′ being located at opposite corners of the rhomb, related by a 2-fold symmetry axis. Fe1 is identified as HS-Fe^{II}, as reflected by the average Fe−N bond distances (d_{Fe-N} = 2.19 Å), while Fe2 is found in the LS-Fe^{II} state (average d_{Fe-N} = 1.97 Å). The extremely distorted geometry for Fe1 can hardly be described as octahedral. On average, the angles deviate from the ideal octahedron by 17%; in some cases the deviation goes up to 45% (N1−Fe1−N13). A more accurate description of the distortion is given by the CSM (continuous symmetry measures) method,[21] which in this case can also be used to characterize HS and LS states since the HS state goes along with a higher distortion.[22] The measures for $[^{Me}L_4Fe^{II}{}_4](BF_4)_4$, with $S(O_h)$ for the octahedron and $S(\text{itp})$ for the trigonal prism, are listed in Table 1, and measures for $[^{H}L_4Fe^{II}{}_4](BF_4)_4$ are included for comparison. A remarkably high value for $S(O_h)$ (corresponding to a lower $S(\text{itp})$) suggests that Fe1 is likely locked in the HS-Fe^{II} state and lacks the ability of facile thermal switching to the LS state. The observed di-mixed-spin configuration [HS−LS−HS−LS], with metal ions of identical spin state located at opposite vertices of the grid, indeed is the sought-after situation for potential QCA applications (compare Figure 1).

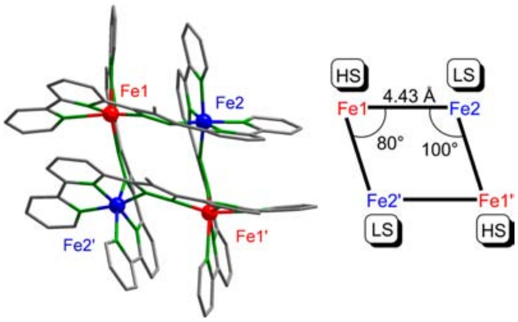

Figure 3. Molecular structure of $[^{Me}L_4Fe^{II}{}_4]^{4+}$ (left; counteranions, H atoms, and solvent molecules omitted for clarity), and schematic representation of the Fe_4 rhomb (right).

Table 1. Mean Fe−N Bond Lengths and Continuous Symmetry Measures (CSM) for $[^{Me}L_4Fe^{II}{}_4](BF_4)_4$ and $[^{H}L_4Fe^{II}{}_4](BF_4)_4$

complex	center	d_{mean}/Å[a]	spin state[a]	$S(O_h)$[b]	$S(\text{itp})$[b]
$[^{Me}L_4Fe^{II}{}_4](BF_4)_4$	Fe1	2.19	HS	8.44	4.89
	Fe2	1.97	LS	2.34	11.1
$[^{H}L_4Fe^{II}{}_4](BF_4)_4$	Fe1	2.17	HS	5.75	7.97
	Fe2	1.99	LS	2.81	9.21
	Fe3	2.18	HS	6.16	7.50
	Fe4	2.19	HS	6.49	7.02

[a] At 133 K. [b] The smaller this value (0−100) the closer the polyhedron is to the ideal geometry.

The UV−vis−NIR spectrum of $[^{Me}L_4Fe^{II}{}_4](BF_4)_4$, recorded in MeCN solution in the range 210−2000 nm, is shown in Figure 4. Three intense bands ($\varepsilon = 7 \times 10^4$ to 12×10^4 L mol^{-1} cm^{-1}) are observed in the high-energy range below 400 nm, likely originating from ligand-based $\pi \rightarrow \pi^*$ transitions. Bands in the visible range and beyond, at 540, 690, and 880 nm ($\varepsilon = 7 \times 10^3$ to 8×10^2 L mol^{-1} cm^{-1}), are tentatively assigned to transitions with largely MLCT character. Basically the same absorptions were observed in a UV−vis spectrum that was measured for a solid sample. Somewhat unexpectedly, however, these MLCT bands are shifted to lower energy compared to those of $[^{H}L_4Fe^{II}{}_4](BF_4)_4$.

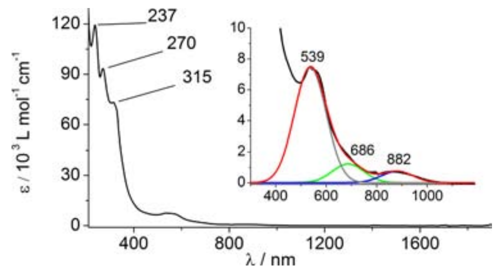

Figure 4. UV−vis−NIR spectrum of $[^{Me}L_4Fe^{II}{}_4](BF_4)_4$. (Inset) Enlargement and deconvolution of the 300−1200 nm range with fitted Gaussian curves.

Magnetic Properties. Susceptibility measurements in the temperature range from 2 to 350 K were performed for a polycrystalline sample of $[^{Me}L_4Fe^{II}{}_4](BF_4)_4$ using a SQUID magnetometer. Over a wide temperature range, between 30 and 250 K, the $\chi_M T$ vs T plot (Figure 5; curve for $[^{H}L_4Fe^{II}{}_4](BF_4)_4$ included for comparison) remains almost constant at around 7.25 cm^3 K mol^{-1}, which corresponds to the spin-only value for two $S = 2$ centers (with $g = 2.20$). This is in accordance with the spin state configuration determined by X-ray crystallography, namely, the presence of two HS-Fe^{II} ($S = 2$) and two LS-Fe^{II} ($S = 0$) ions. Below 30 K, $\chi_M T$ drops rapidly; if one assumes that any magnetic coupling between the diagonally opposed HS-Fe^{II} spin carriers in the molecule is negligible,[23] this drop of $\chi_M T$ is likely due to zero-field splitting. Data points below 200 K were indeed well simulated assuming two

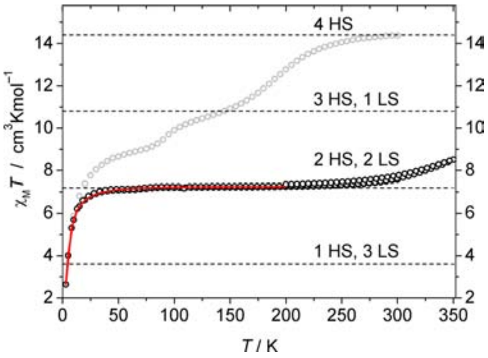

Figure 5. $\chi_M T$ vs T of $[^{Me}L_4Fe^{II}{}_4](BF_4)_4$ (black circles) and $[^{H}L_4Fe^{II}{}_4](BF_4)_4$ (gray circles). Red line is the best simulation for data points below 200 K (see text and Supporting Information).

uncoupled $S = 2$ centers, with an axial zero field splitting parameter $|D| = 11.4\ \mathrm{cm^{-1}}$ and Zeeman splitting (red solid line in Figure 5; spin Hamiltonian given in eq 1; see Supporting Information for details).[24]

$$\hat{H} = \sum_{i=1}^{2} \left(D\left(\hat{S}_{zi}^{2} - 1/3S_i(S_i + 1)\right) + g\mu_{\mathrm{B}}\vec{B}\cdot\vec{S_i}\right) \tag{1}$$

Above 200 K, $\chi_M T$ increases gradually to reach 8.5 cm^3 K mol^{-1} at 350 K, which likely indicates the onset of a spin transition. A subsequent measurement in the cooling mode shows a similar but slightly incongruent curvature, which may reflect some change of the sample material after heating to 350 K, e.g., solvent loss.

The pronounced stabilization of the di-mixed-spin configuration [HS–LS–HS–LS] in $[^{Me}L_4Fe^{II}{}_4](BF_4)_4$, which prevents SCO over a large temperature range, is not only caused by the slightly stronger ligand field of $[^{Me}L]^-$ compared to parent $[^{H}L]^-$ but can be rationalized on the basis of structural peculiarities. It is well known that HS-Fe^{II} ions have a strong tendency to remain in that spin state if their coordination sphere is strongly distorted from ideal octahedral symmetry.[25,26] The $S(O_h)$ value[22] of the HS-Fe^{II} ions in $[^{Me}L_4Fe^{II}{}_4](BF_4)_4$ indeed is distinctly higher than in $[^{H}L_4Fe^{II}{}_4](BF_4)_4$ (see Table 1). Additionally, recent DFT calculations examining different spin states of $[^{H}L_4Fe^{II}{}_4](BF_4)_4$ revealed that increased strain in the overall grid structure, induced by ligand distortion away from planarity, can suppress the spin transition.[23] Indeed, in $[^{Me}L_4Fe^{II}{}_4](BF_4)_4$ the average angles between the planes of the pyrazolates and their neighboring pyridine rings are 16.7° (at HS-Fe^{II} sites) and 12.6° (at LS-Fe^{II} sites), which reflects much greater ligand distortion than in $[^{H}L_4Fe^{II}{}_4](BF_4)_4$ (7.2° and 4.0°, respectively). Steric demands of the backbone methyl group in $[^{Me}L]^-$ may in part be responsible for the larger torsion angle between the pyrazole ring and the appended 2,2′-bipyridyl groups.

Mössbauer Spectroscopy. ^{57}Fe Mössbauer spectroscopy is a valuable tool for assessing spin and charge states of iron atoms. Spectra of solid $[^{Me}L_4Fe^{II}{}_4](BF_4)_4$ were recorded at six different temperatures between 7 and 300 K; the results for three selected temperatures (7, 150, 250 K) are shown in Figure 6 (the other spectra are shown in the Supporting Information). In all cases, the spectra feature two quadrupole doublets with equal area fractions, confirming the presence of two types of iron atoms. Mössbauer parameters are collected in Table 2. At 250 K, the characteristic subspectra for HS-Fe^{II} (red doublet, $\delta = 0.96$ mm/s, $\Delta E_Q = 1.30$ mm/s) and LS-Fe^{II} (blue doublet, $\delta = 0.31$ mm/s, $\Delta E_Q = 0.96$ mm/s) are well separated. Upon cooling, the parameters for the LS doublet remain almost constant, while the parameters for the HS doublet change significantly: the isomeric shift increases slightly to 1.08 mm/s at 7 K, while the quadrupole splitting increases considerably to 2.13 mm/s. Thus, the doublets superimpose more and more until at 7 K only three distinct peaks are remaining.

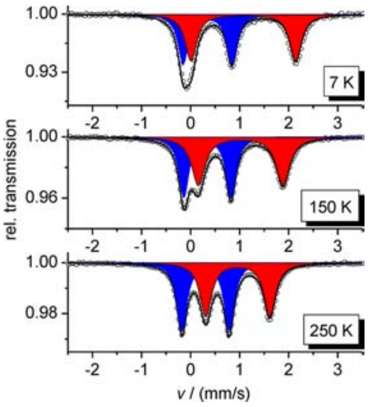

Figure 6. Zero-field ^{57}Fe Mössbauer spectra for solid $[^{Me}L_4Fe^{II}{}_4](BF_4)_4$ at different temperatures. Lines represent simulations with Lorentzian doublets for HS-Fe^{II} (red doublet) and LS-Fe^{II} (blue doublet).

Table 2. Mössbauer Parameters for $[^{Me}L_4Fe^{II}{}_4](BF_4)_4$

T/K	Fe species	δ (mm/s)	ΔE_Q (mm/s)	area (%)
7[a]	LS-Fe^{II}	0.35	0.99	48.0
	HS-Fe^{II}	1.08	2.13	52.2
80[a]	LS-Fe^{II}	0.35	0.98	48.3
	HS-Fe^{II}	1.06	2.07	51.7
150[a]	LS-Fe^{II}	0.34	0.96	47.5
	HS-Fe^{II}	1.02	1.73	52.5
200[a]	LS-Fe^{II}	0.33	0.96	49.8
	HS-Fe^{II}	0.99	1.48	50.2
250[a]	LS-Fe^{II}	0.31	0.96	51.6
	HS-Fe^{II}	0.96	1.30	48.4
295[a]	LS-Fe^{II}	0.28	0.96	50.2
	HS-Fe^{II}	0.94	1.17	49.8
80[b]	LS-Fe^{II}	0.32	0.94	72.5
	HS-Fe^{II}	1.10	2.44	27.5

[a] Solid sample. [b] In frozen MeCN solution.

The changes in quadrupole splitting can be readily explained by a minor valence contribution. Assuming that the Jahn–Teller splitting energy Δ has a similar magnitude as the thermal energy, population of the involved orbitals follows a Boltzmann distribution. Which specific levels are populated at lower temperatures is not clear yet. With respect to Δ, the temperature dependence of ΔE_Q follows eq 2.[27]

$$\Delta E_Q(T) = \Delta E_Q(0)\cdot\frac{1 - \exp(-\Delta/kT)}{1 + \exp(-\Delta/kT)} \tag{2}$$

The temperature dependence of the isomeric shift is caused by the second-order Doppler effect (SOD). δ decreases with rising temperatures according to eq 3 that is based on a Debye model.[27]

$$\delta_{\mathrm{SOD}} = -\frac{9k_{\mathrm{B}}E}{16M_{\mathrm{eff}}c^2}\left(\Theta_{\mathrm{M}} + 8T\left(\frac{T}{\Theta_{\mathrm{M}}}\right)^3\cdot\int_0^{\Theta_{\mathrm{M}}/T}\frac{x^3}{e^x - 1}\mathrm{d}x\right) \tag{3}$$

Variation of the parameters Θ_M (Mössbauer temperature, reflecting the “solidity” of the material), M_{eff} (effective mass), and x (displacement of the nucleus) gives the fitting curves and parameters shown in Figure 7. As expected, Θ_M is higher for LS-Fe^{II} because of a higher bond order and the resulting shorter Fe–N bonds.

In addition to measurements on solid samples, Mössbauer spectra of frozen MeCN solutions of $[^{Me}L_4Fe^{II}{}_4](BF_4)_4$ were recorded at two temperatures (80 and 180 K). The spectrum collected at 80 K, depicted in Figure 8 (top), shows the characteristic subspectra for LS-Fe^{II} (blue) and HS-Fe^{II} (red). However, the ratio of LS and HS changed to 3:1 in solution (compared to 2:2 in the solid state), which evidences a [1HS–

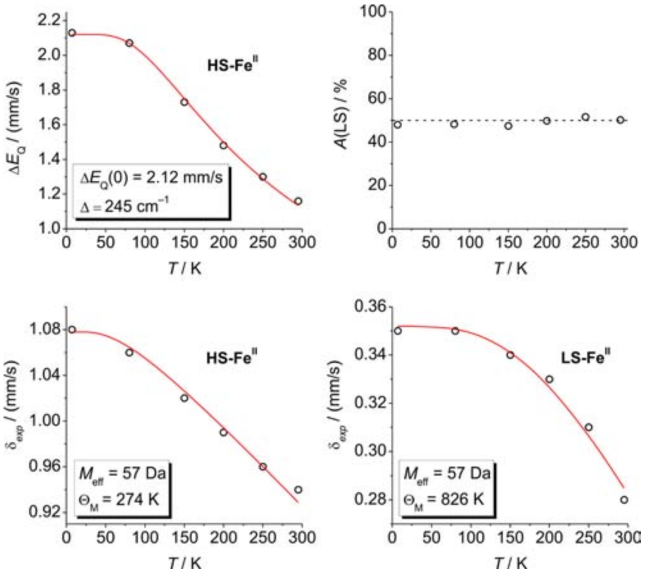

Figure 7. Temperature dependence of Mössbauer parameters for $[^{Me}L_4Fe^{II}_4](BF_4)_4$: quadrupole splitting of the HS state (top left), relative peak area of the LS state (top right), and isomer shift of the HS state (bottom left) and LS state (bottom right). Red lines represent the best simulations using eqs 1 and 2 with the parameters given as insets; dotted line in the top right graph represents the 50% line as a guide for the eye.

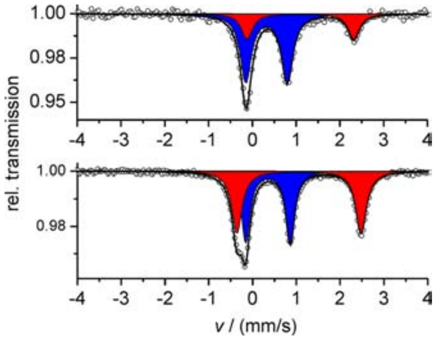

Figure 8. Zero-field ^{57}Fe Mössbauer spectra for $[^{Me}L_4Fe^{II}_4](BF_4)_4$ in frozen MeCN solution (top) and for $[^{H}L_4Fe^{II}_4](BF_4)_4$ in frozen DMF solution (bottom), both measured at 80 K. Lines represent simulations with Lorentzian doublets for HS-Fe^{II} (red doublet) and LS-Fe^{II} (blue doublet).

3LS] configuration for the Fe$^{II}_4$ grid. The preference of the LS state for solution samples using donor solvents such as MeCN is well documented[28] and usually attributed to H bonding between the solvent molecules and the ligands or to different dissociation equilibria.[29] Both effects are likely not relevant for the present complex; rather we consider the reduced ligand field strength as a solid state phenomenon. For comparison, the previously reported parent grid complex $[^{H}L_4Fe^{II}_4](BF_4)_4$[19] was now investigated by Mössbauer spectroscopy in frozen solution (Figure 8, bottom). Also, in this case the LS fraction increases, namely, from [3HS−1LS] in the solid state at 80 K to [2HS−2LS] in frozen DMF.

Redox Properties. Redox properties of $[^{Me}L_4Fe^{II}_4]^{4+}$ were investigated by cyclic voltammetry in MeCN solution. Four anodic processes have been detected in the potential range from −0.2 to +1.8 V (vs SCE; Table 3), suggesting sequential oxidation of the all-ferrous grid to all-ferric $[^{Me}L_4Fe^{III}_4]^{8+}$ (Figure 9). The first three processes **a**−**c** are chemically reversible, while the fourth couple seems to have limited chemical reversibility, likely because of instability of the 4-fold oxidized and highly charged species $[^{Me}L_4Fe^{III}_4]^{8+}$. All four couples **a**−**d** are electrochemically quasi-reversible (peak separations $\Delta E_p \approx 105$ mV for **a** and **b**, $\Delta E_p \approx 135$ mV for **c** and **d**; $\Delta E_p = 75$ mV was found for the internal standard Cp^*_2Fe).

Table 3. Electrochemical Parameters for $[^{Me}L_4Fe^{II}_4](BF_4)_4$ and $[^{H}L_4Fe^{II}_4](BF_4)_4$

	$E_{1/2}$/ mV	ΔE_p/ mV^a	oxidized species	K_c	$E_{1/2}$/mV for $[^{H}L_4Fe_4]^{4+}$ [19]
a	518	102	$[^{Me}L_4Fe^{II}_3Fe^{III}]^{5+}$	4.41×10^2	642
b	674	108	$[^{Me}L_4Fe^{II}_2Fe^{III}_2]^{6+}$	3.35×10^8	783
c	1177	135	$[^{Me}L_4Fe^{II}Fe^{III}_3]^{7+}$	6.26×10^3	1257
d	1401	138	$[^{Me}L_4Fe^{III}_4]^{8+}$		1438

^{a}Separation of anodic and cathodic peak potentials.

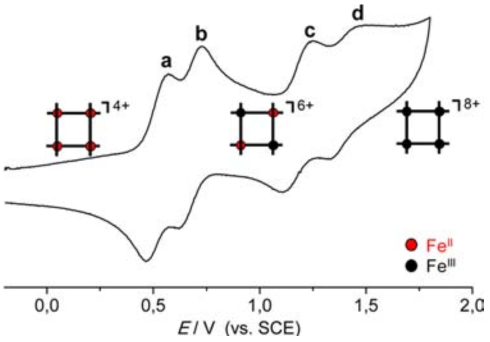

Figure 9. Cyclic voltammogram of $[^{Me}L_4Fe^{II}_4](BF_4)_4$ in MeCN/0.1 M NBu_4PF_6 referenced against SCE at a scan rate of 1000 mV/s. Decamethylferrocene couple $Cp^*_2Fe/Cp^*_2Fe^+$ was used as internal standard (not shown).

The sequence of redox steps for $[^{Me}L_4Fe^{II}_4]^{4+}$ is most likely analogous to that previously seen for $[^{H}L_4Fe^{II}_4]^{4+}$.[19] The cyclic voltammogram can be subdivided into two pairs of anodic processes. The pair **a**/**b** is assigned to oxidations at diagonally opposed positions of the rhomb. In the resulting $[^{Me}L_4Fe^{II}_2Fe^{III}_2]^{6+}$ each ferric ion still has two ferrous ions as neighbors, resulting in high thermodynamic stability of the di-mixed-valent species (comproportionation constant $K_C = 3.35 \times 10^8$, similar to the value found for parent $[^{H}L_4Fe^{II}_4]^{4+}$).[19] Oxidation of the third grid vertex is significantly more demanding, and hence, the pair **c**/**d**, assigned to sequential oxidation of the remaining two Fe^{II} ions, follows after a relatively large potential gap. In this picture the differentiation into two pairs is readily explained by electrostatic interaction between neighboring corners of the grid.[30] Overall the potentials of the individual oxidation processes are significantly lower than for complex $[^{H}L_4Fe^{II}_4]^{4+}$ (see Table 3). This can be explained, similar to the ligand-field effect, by the electron-donating effect of the backbone methyl group of the ligand, which stabilizes the Fe^{II} state. Interestingly, the difference between $[^{Me}L_4Fe_4]^{x+}$ and $[^{H}L_4Fe_4]^{x+}$ becomes smaller the more oxidized the grids are (Δ is 124 mV for couple **a** but only 37 mV for couple **d**).

■ CONCLUSIONS

Building upon our recent report of a robust pyrazolate-bridged Fe$_4$ [2 × 2] grid complex,[19] we have now modified the pyrazolate-derived ligand scaffold to slightly increase the ligand field strength. This has furnished a new Fe_4 [2 × 2] grid, $[^{Me}L_4Fe^{II}_4](BF_4)_4$, that has SCO and redox properties optimized for use as QCA. In the solid state, $[^{Me}L_4Fe^{II}_4](BF_4)_4$ adopts a di-mixed-spin configuration [HS−LS−HS−LS] over a wide temperature range, with Fe^{II} ions of the same spin state located at diagonally opposed vertices of the grid. Furthermore, $[^{Me}L_4Fe^{II}_4]^{4+}$ is more easily oxidized than parent $[^{H}L_4Fe^{II}_4]^{4+}$, and the 2-fold oxidized species $[^{Me}L_4Fe^{II}_2Fe^{III}_2]^{6+}$ has favorably high stability with respect to disproportionation. The sequence of redox events suggests that identical Fe ions in $[^{Me}L_4Fe^{II}_2Fe^{III}_2]^{6+}$, having the same charge state, are again located at diagonally opposed vertices of the grid. Such configuration is indeed required for potential implementation in QCA devices, in which binary information is encoded by means of the spin or charge configuration of quantum-dot cells rather than any current flow. QCA represent a new computing platform at the nanotechnology level for which molecular representatives are highly sought.[5] Experiments aimed at depositing and manipulating molecules of the new Fe_4 [2 × 2] grid on surfaces as well as experiments aimed at bistable charge or spin switching of the grid are planned.

■ EXPERIMENTAL SECTION

Methods and Materials. Some steps of the synthesis of ^{Me}LH as well as the synthesis of $[^{Me}L_4Fe^{II}_4](BF_4)_4$ were carried out under an inert atmosphere of dry argon or dinitrogen (see below). All other manipulations were carried out in air. Acetonitrile and diethyl ether were used in HPLC grade and other solvents in reaction grade. 6-Cyano-2,2′-bipyridine,[20] 6-(2,2′-bipyridyl)methylcarboxylate (**I**),[20] 6-acetyl-2,2′-bipyridine (**III**),[20] as well as the parent complex $[^{H}L_4Fe^{II}_4](BF_4)_4$[19] were synthesized according to literature procedures. All other chemicals were used as purchased or their synthesis is described below.

NMR spectra were recorded on Bruker Avance 200 and 300 MHz spectrometers and referenced to the residual solvent signal: $\delta(CDCl_3) = 7.24$ (^1H) and 77.1 (^{13}C) ppm. UV−vis−NIR spectra were measured on a Varian Cary 5000. Mössbauer data were collected with a ^{57}Co source embedded in a Rh matrix using an alternating constant acceleration Wissel Mössbauer spectrometer operated in the transmission mode and equipped with a Janis closed-cycle helium cryostat. Isomer shifts are given relative to iron metal at ambient temperature. Simulation of the experimental data was performed with the *Mfit* program.[31] Temperature-dependent magnetic susceptibilities were measured using a SQUID magnetometer (Quantum Design MPMS-XL-5) at 0.2 T. Cyclic voltammetry was performed at room temperature with a potentiostat/galvanostat Perkin-Elmer model 263A with a glassy carbon working electrode and platinum reference and counter electrodes in MeCN/0.1 M NBu_4PF_6. Decamethylferrocene was used as internal standard. ESI-MS spectra were recorded on a BRUKER HCT Ultra instrument and EI-MS spectra on a Finnigan MAT 8200.

6-Propionyl-2,2′-bipyridine (II). Ethyl magnesium bromide (1 M in THF, 33.2 mL, 33.2 mmol) was added dropwise to a solution of 6-cyano-2,2′-bipyridine (5.00 g, 27.6 mmol) in diethyl ether (70 mL) at −15 °C under an atmosphere of dry argon. The reaction mixture was stirred at −15 °C for 30 min and warmed to room temperature over 1 h. After careful addition of hydrochloric acid (5 mL, 2 M) and diethyl ether (30 mL), the aqueous phase was separated and extracted with dichloromethane (3 × 50 mL). Combined organic phases were washed with water (2 × 50 mL) and dried over $MgSO_4$. After removal of the solvents, the crude product was purified by column filtration over aluminum oxide with dichloromethane. After removal of the solvent, a yellow solid was obtained (3.32 g, 15.6 mmol, 56.7%). ^1H NMR (300 MHz, $CDCl_3$): $\delta = 8.70$ (ddd, $J = 4.9, 1.8, 0.9$ Hz, 1H), 8.61 (dd, $J = 7.8, 1.2$ Hz, 1H), 8.53 (dt, $J = 8.0, 1.1$ Hz, 1H), 8.05 (dd, $J = 7.7, 1.2$ Hz, 1H), 7.95 (t, $J = 7.8$ Hz, 1H), 7.86 (ddd, $J = 8.0, 7.5, 1.8$ Hz, 1H), 7.35 (ddd, $J = 7.6, 4.8, 1.2$ Hz, 1H), 3.38 (q, $J = 7.3$ Hz, 2H), 1.28 (t, $J = 7.3$ Hz, 3H) ppm. ^{13}C NMR (75 MHz, $CDCl_3$) $\delta = 8.20$, 31.26, 121.27, 121.67, 124.23, 124.32, 137.11, 137.97, 149.39, 152.94, 155.48, 155.65, 202.86 ppm.

1,3-Bis{6-(2,2′-bipyridyl)}-1,3-propandione (IV). Under an atmosphere of dinitrogen 6-(2,2′-bipyridyl)methylcarboxylate (2.00 g, 9.35 mmol) and 6-acetyl-2,2′-bipyridine (1.85 g, 9.35 mmol) were dissolved in 1,4-dioxane (25 mL). A suspension of sodium methoxide (0.55 g, 10.3 mmol) in 1,4-dioxane (5 mL) was added, and the solution was stirred at room temperature for 5 h. A solution of hydrochloric acid in water (2 M, 5 mL) was added, and the precipitate was separated by filtration, washed with water (100 mL), and dried. The solid was dissolved in chloroform (100 mL) and saturated aqueous sodium bicarbonate solution (100 mL), and the organic phase was then separated. The aqueous phase was extracted with chloroform (3 × 100 mL), and the combined organic phases were dried over Na_2SO_4. After removal of the solvent, a white solid (2.94 g, 7.74 mmol, 83%) was obtained. The product can be further purified by recrystallization from toluene or methanol yielding the pure enol form. The corresponding keto form was only obtained in a mixture with the enol form.

Enol Form. ^1H NMR (200 MHz, $CHCl_3$): $\delta = 15.80$ (s, 1H), 8.80−8.68 (m, 4H), 8.63 (dd, $J = 7.9, 1.1$ Hz, 2H), 8.57 (s, 1H), 8.20 (dd, $J = 7.7, 1.1$ Hz, 2H), 8.02 (t, $J = 7.8$ Hz, 2H), 7.89 (td, $J = 7.6, 1.8$ Hz, 2H), 7.46−7.33 (m, 2H) ppm. ^{13}C NMR (75 MHz, $CDCl_3$) $\delta = 94.82$, 121.33, 122.13, 123.77, 124.25, 136.82, 138.13, 149.40, 151.78, 155.71, 155.75, 184.25 ppm.

Keto Form. ^1H NMR (300 MHz, $CDCl_3$): $\delta = 8.65$−8.57 (m, 2H), 8.56−8.50 (m, 2H), 8.21−8.12 (m, 2H), 8.07 (dd, $J = 7.7, 1.1$ Hz, 2H), 7.91−7.81 (m, 2H), 7.67 (td, $J = 7.8, 1.8$ Hz, 2H), 7.31−7.20 (m, 2H), 4.81 (s, 2H) ppm. ^{13}C NMR (75 MHz, $CDCl_3$) $\delta = 50.34$, 121.36, 122.04, 124.29, 124.41, 137.17, 138.24, 149.23, 152.03, 154.97, 155.65, 195.83 ppm.

1,3-Bis{6-(2,2′-bipyridyl)}-2-methyl-1,3-propandione (V). Under an atmosphere of dinitrogen 1,3-bis{6-(2,2′-bipyridyl)}-1,3-propandione (3.35 g, 8.79 mmol) and potassium bis(trimethylsilyl)-amide (2.63 g, 13.2 mmol) were suspended in toluene (150 mL). The green suspension was heated to 70−80 °C, and methyl iodide (2.7 mL, 44 mmol) was added. The mixture was heated to reflux for 4 h; the color of the reaction mixture changed to yellow during this period. A white solid was filtered off and washed with toluene (10 mL). The filtrate was washed with saturated aqueous sodium bicarbonate solution (100 mL) and water (100 mL). The combined aqueous phases were extracted with chloroform (3 × 75 mL), and the combined organic phases were dried over Na_2SO_4. After removal of the solvent, a white solid (3.37 g, 8.55 mmol, 97%) was obtained. ^1H NMR (300 MHz, $CDCl_3$): $\delta = 8.65$−8.54 (m, 2H), 8.49 (dd, $J = 7.9, 1.0$ Hz, 2H), 8.13−8.00 (m, 4H), 7.82 (t, $J = 7.8$ Hz, 2H), 7.68 (td, $J = 7.8, 1.8$ Hz, 2H), 7.34−7.17 (m, 2H), 5.33 (q, $J = 7.0$ Hz, 1H), 1.71 (d, $J = 7.0$ Hz, 3H) ppm. ^{13}C NMR (75 MHz, $CDCl_3$) $\delta = 13.56$, 52.17, 121.41, 122.27, 124.14, 124.24, 137.20, 138.26, 149.17, 151.50, 154.98, 155.53, 198.17 ppm.

1,3-Bis{6-(2,2′-bipyridyl)}-2-methyl-1,3-propandione (V) and 4-Methyl-3,5-bis{6-(2,2′-bipyridyl)}pyrazole (^{Me}LH) via Route 1. Potassium hydride was added to a solution of 6-(2,2′-bipyridyl)-methylcarboxylate (3.00 g, 14.0 mmol) in toluene (10 mL) under an atmosphere of dry argon. After heating this mixture to around 70−80 °C, a solution of 6-propionyl-2,2′-bipyridine (3.00 g, 14.1 mmol) in toluene (7 mL) was added dropwise and the resulting mixture stirred for 1 h. The solution was then slowly cooled down to room temperature over 1 h, and a mixture of acetic acid and ethanol (10 mL, 1:1) was added. A precipitate formed and was separated by filtration and washed with cold ethanol (2 × 5 mL). After drying, 1,3-bis{6-(2,2′-bipyridyl)}-2-methyl-1,3-propandione was obtained as a bright yellow solid (1.52 g, 3.85 mmol), which was used without further purification. It was suspended in ethanol (20 mL), and hydrazine hydrate (0.30 mL, 5.87 mmol) was added. The mixture was heated to reflux for 1 h. After cooling to room temperature a precipitate formed and was separated by filtration and washed with ethanol (2 × 10 mL). A second crop was obtained by removal of the solvent of the filtrate. After drying under reduced pressure, the product ^{Me}LH was obtained as an off-white solid (1.47 g, 3.77 mmol, 27% over two steps). Spectral data were identical to material prepared via route 2; for characterization data see below.

4-Methyl-3,5-bis{6-(2,2′-bipyridyl)}pyrazole (^{Me}LH) via Route 2. 1,3-Bis{6-(2,2′-bipyridyl)}-2-methyl-1,3-propandione (3.37 g, 8.55 mmol) was dissolved in ethanol (50 mL), and hydrazine hydrate (2.5 mL, 51 mmol) was added. The mixture was heated to reflux for 3 h. A precipitate formed when the mixture was cooled to room temperature, separated by filtration, and washed with water. After drying a white solid (2.03 g, 5.21 mmol, 61%) was obtained. ^{1}H NMR (200 MHz, $CDCl_3$): δ = 8.75−8.63 (m, 2H), 8.55−8.42 (m, 2H), 8.42−8.27 (m, 2H), 7.97−7.70 (m, 6H), 7.36−7.21 (m, 2H), 2.91 (s, 3H) ppm. ^{13}C NMR (75.4 MHz, $CDCl_3$): δ = 11.30, 113.82, 119.57, 121.18, 123.83, 136.96, 137.69, 149.16, 155.48, 156.06 ppm. EI-MS: m/z (%) = 390 (100) $[M]^+$. UV−vis (MeCN): λ_{max}/nm (ε/(L mol^{-1} cm^{-1})) = 237 (5.3 × 10^4), 266 (4.9 × 10^4), 303 (3.5 × 10^4). Anal. Calcd for $C_{24}H_{18}N_6$: C, 73.83; H, 4.65; N, 21.52. Found: C, 73.30; H, 4.70; N, 21.32.

$[^{Me}L_4Fe^{II}_4](BF_4)_4$. The proligand ^{Me}LH (300 mg, 768 μmol) together with NaOtBu (74 mg, 768 μmol) was stirred in DMF (20 mL) for 15 min. The resulting bright-yellow solution was added dropwise to a solution of $Fe(BF_4)_2\cdot 6H_2O$ (260 mg, 768 μmol) in degassed methanol (10 mL). The solution gradually turned deep red and was stirred overnight at room temperature The reaction mixture was then poured into stirred diethyl ether (300 mL) and further stirred for 30 min. After sedimentation, the main part of the solvent was decanted. The residue was washed repeatedly in the same way (3 × 100 mL). The resulting red-brown powder was subsequently dried in vacuo. This powder was suspended with acetone (300 mL), sonicated for 15 min, and stirred for 1 h. The suspension was filtered over Celite; the greenish forerunnings were discarded. Acetone was removed under reduced pressure at 30 °C. A black solid material (260 mg, 120 μmol, 64%) was obtained, which was finally crystallized by slow diffusion of diethyl ether into a solution of the crude complex in MeCN. ESI-MS (ESI$^+$, MeCN): m/z (%) = 445 $[Fe_4L_4]^{4+}$ superimposed by $[Fe_2L_2]^{2+}$. UV−vis (MeCN): λ_{max}/nm (ε/(L mol^{-1} cm^{-1})) = 237 (120 000), 270 (92 000), 315 (70 000), 540 (7000), 690 (1000), 870 (800). Anal. Calcd for $(C_{24}H_{17}N_6)_4Fe_4(BF_4)_4$: C, 54.18; H, 3.22; N, 15.79. Found: C, 53.33; H, 3.70; N, 16.52.

■ ASSOCIATED CONTENT

Ⓢ Supporting Information

Crystallographic data and plot of the molecular structure with anisotropic displacement ellipsoids; variable-temperature Mössbauer spectra; NMR spectra of all new compounds. This material is available free of charge via the Internet at http://pubs.acs.org.

■ AUTHOR INFORMATION

Corresponding Author

*E-mail: franc.meyer@chemie.uni-goettingen.de.

Notes

The authors declare no competing financial interest.

■ ACKNOWLEDGMENTS

Financial support by the Deutsche Forschungsgemeinschaft (SFB 602 and Me 1313/9-1) and the State of Lower Saxony (International Ph.D. program Catalysis for Sustainable Synthesis, CaSuS) is gratefully acknowledged.

■ REFERENCES

(1) (a) Coskun, A.; Spruell, J. M.; Barin, G.; Dichtel, W. R.; Flood, A. H.; Botros, Y. Y.; Stoddart, J. F. *Chem. Soc. Rev.* **2012**, *41*, 4827−4859. (b) Ratner, M. *Nat. Nanotechnol.* **2013**, *8*, 378−381. (c) Low, P. J. *Dalton Trans.* **2005**, 2821−2824.

(2) Minkin, V. I. *Russ. Chem. Bull.* **2008**, *57*, 687−717.

(3) (a) Létard, J.-F.; Guionneau, P.; Goux-Capes, L. *Top. Curr. Chem.* **2004**, *235*, 221−249. (b) Kahn, O.; Martinez, C. J. *Science* **1998**, *279*, 44−48. (c) Gütlich, P.; Hauser, A.; Spiering, H. *Angew. Chem., Int. Ed.* **1994**, *33*, 2024−2054. (d) Toftlund, H. *Coord. Chem. Rev.* **1989**, *94*, 67−108.

(4) (a) Tougaw, P. D.; Lent, C. S. *J. Appl. Phys.* **1994**, *75*, 1818−1825. (b) Amlani, I.; Orlov, A. O.; Toth, G.; Bernstein, G. H.; Lent, C. S.; Snider, G. L. *Science* **1999**, *284*, 289−291.

(5) Lu, Y.; Lent, C. S. *Nanotechnology* **2008**, *19*, 155703 + 11.

(6) (a) Lent, C. S.; Tougaw, P. D.; Porod, W.; Bernstein, G. H. *Nanotechnology* **1993**, *4*, 49−57. (b) Lent, C. S.; Tougaw, P. D. *Proc. IEEE* **1997**, *85*, 541−557.

(7) (a) Lent, C. S. *Science* **2000**, *288*, 1597−1599. (b) Lent, C. S.; Isaksen, B.; Lieberman, M. *J. Am. Chem. Soc.* **2003**, *125*, 1056−1063.

(8) Wang, X.; Ma, J. *Phys. Chem. Phys. Chem.* **2011**, *13*, 16134−16137.

(9) (a) Jiao, J.; Long, G. J.; Grandjean, F.; Beatty, A. M.; Fehlner, T. P. *J. Am. Chem. Soc.* **2003**, *125*, 7522−7523. (b) Jiao, J.; Long, G. J.; Rebbouh, L.; Grandjean, F.; Beatty, A. M.; Fehlner, T. P. *J. Am. Chem. Soc.* **2005**, *127*, 17819−17831.

(10) Braun-Sand, S. B.; Wiest, O. *J. Phys. Chem. A* **2003**, *107*, 285−291.

(11) Robin, M. B.; Day, P. *Adv. Inorg. Chem. Radiochem.* **1967**, *10*, 247−422.

(12) Ruben, M.; Rojo, J.; Romero-Salguero, F. J.; Uppadine, L. H.; Lehn, J. M. *Angew. Chem., Int. Ed.* **2004**, *43*, 3644−3662.

(13) (a) Dawe, L. N.; Abedin, T. S. M.; Thompson, L. K. *Dalton Trans.* **2008**, 1661−1675. (b) Dawe, L. N.; Shuvaev, K. V.; Thompson, L. K. *Chem. Soc. Rev.* **2009**, *38*, 2334−2359. (c) Stadler, A.-M. *Eur. J. Inorg. Chem.* **2009**, 4751−4770.

(14) (a) Breuning, E.; Ruben, M.; Lehn, J.-M.; Renz, F.; Garcia, Y.; Ksenofontov, V.; Gütlich, P.; Wegelius, E.; Rissanen, K. *Angew. Chem., Int. Ed.* **2000**, *39*, 2504−2507. (b) Ruben, M.; Breuning, E.; Lehn, J.-M.; Ksenofontov, V.; Renz, F.; Gütlich, P.; Vaughan, G. B. M. *Chem.—Eur. J.* **2003**, *9*, 4422−4429. (c) Ruben, M.; Ziener, U.; Lehn, J.-M.; Ksenofontov, V.; Gütlich, P.; Vaughan, G. B. M. *Chem.—Eur. J.* **2005**, *11*, 94−100. (d) Uppadine, L. H.; Gisselbrecht, J.-P.; Kyritsakas, N.; Nättinen, K.; Rissanen, K.; Lehn, J.-M. *Chem.—Eur. J.* **2005**, *11*, 2549−2565. (e) Wang, Y.-T.; Li, S.-T.; Wu, S.-Q.; Cui, A.-L.; Shen, D.-Z.; Kou, H.-Z. *J. Am. Chem. Soc.* **2013**, *135*, 5942−5945.

(15) (a) Nihei, M.; Ui, M.; Yokota, M.; Han, L.; Maeda, A.; Kishida, H.; Okamoto, H.; Oshio, H. *Angew. Chem., Int. Ed.* **2005**, *44*, 6484−6487. (b) Boldog, I.; Muñoz-Lara, F. J.; Gaspar, A. B.; Muñoz, M. C.; Seredyuk, M.; Real, J. A. *Inorg. Chem.* **2009**, *48*, 3710−3719. (c) Mondal, A.; Li, Y.; Herson, P.; Seuleiman, M.; Boillot, M.-L.; Rivière, E.; Julve, M.; Rechignat, L.; Bousseksou, A.; Lescouëzec, R. *Chem. Commun.* **2012**, *48*, 5653−5655.

(16) (a) Gang, H.; Dong, G.; Chun-Ying, D.; Hong, M.; Qing-jin, M. *New J. Chem.* **2002**, *26*, 1371−1377. (b) Zhao, Y.; Guo, D.; Liu, Y.; He, C.; Duan, C. *Chem. Commun.* **2008**, 5725−5727. Shuvaev, K. V.; Dawe, L. N.; Thompson, L. K. *Dalton Trans.* **2010**, *39*, 4768−4776.

(17) (a) Wu, D.-Y.; Sato, O.; Einaga, Y.; Duan, C.-Y. *Angew. Chem., Int. Ed.* **2009**, *48*, 1475−1478. (b) Wei, R.-J.; Huo, Q.; Tao, J.; Huang, R.-B.; Zheng, L.-S. *Angew. Chem., Int. Ed.* **2011**, *50*, 8940−8943.

(18) Li, F.; Clegg, J. K.; Goux-Capes, L.; Chastanet, G.; D'Alessandro, D. M.; Létard, J.-F.; Kepert, C. J. *Angew. Chem.* **2011**, *123*, 2872−2875; *Angew. Chem., Int. Ed.* **2011**, *50*, 2820−2823.

(19) Schneider, B.; Demeshko, S.; Dechert, S.; Meyer, F. *Angew. Chem., Int. Ed.* **2010**, *49*, 9274−9277.

(20) van der Vlugt, J. I.; Demeshko, S.; Dechert, S.; Meyer, F. *Inorg. Chem.* **2008**, *47*, 1576−1585.

(21) (a) Alvarez, S.; Avnir, D.; Llunell, M.; Pinsky, M. *New J. Chem.* **2002**, *26*, 996−1009. (b) Zabrodsky, H.; Peleg, S.; Avnir, D. *J. Am. Chem. Soc.* **1992**, *114*, 7843−7851. (c) Zabrodsky, H.; Peleg, S.; Avnir, D. *J. Am. Chem. Soc.* **1993**, *115*, 8278−8289.

(22) Alvarez, S. *J. Am. Chem. Soc.* **2003**, *125*, 6795−6802.

(23) Borshch, S. A.; Zueva, E. M. *Eur. J. Inorg. Chem.* **2013**, *18*, 1009−1014.

(24) Full-matrix diagonalization of the spin Hamiltonian for zero-field splitting and Zeeman splitting was performed with the *julX* program (Max-Planck Institute for Chemical Energy Conversion, Mülheim/Ruhr, Germany).

(25) Halcrow, M. A. *Chem. Soc. Rev.* **2011**, *40*, 4119−4142.

(26) Craig, G. A.; Costa, J. S.; Roubeau, O.; Teat, S. J.; Aromí, G. *Chem.—Eur. J.* **2012**, *18*, 11703−11715.

(27) P. Gütlich, Bill, E.; Trautwein, A. X. *Mössbauer Spectroscopy and Transition Metal Chemistry*; Springer-Verlag: Berlin, Heidelberg, 2011.

(28) (a) Strauss, B.; Gutmann, V.; Linert, W. *Monatsh. Chem.* **1993**, *124*, 515−522. (b) Linert, W.; Enamullah, M.; Gutmann, V.; Jameson, R. F. *Monatsh. Chem.* **1994**, *125*, 661−670.

(29) Nitschke, J. R.; Lehn, J.-M. *Proc. Natl. Acad. Sci.* **2003**, *100*, 11970−11974.

(30) (a) Bassani, D. M.; Lehn, J.-M.; Serroni, S.; Puntoriero, F.; Campagna, S. *Chem.—Eur. J.* **2003**, *9*, 5936−5946. (b) Ruben, M.; Breuning, E.; Barboiu, M.; Gisselbrecht, J.; Lehn, J.-M. *Chem.—Eur. J.* **2003**, *9*, 291−299.

(31) Bill, E. *Mfit*; Max-Planck Institute for Chemical Energy Conversion, Mülheim/Ruhr, Germany, 2008.